Journal of Civil Engineering and Construction 2025;14(2):71-87
https://doi.org/10.32732/jcec.2025.14.2.71

One-Way Fluid–Structure Coupled Analysis of a Construction Scaffolding under Wind Loads

Daigoro Isobe[1], Takumi Tago[2]

1. Division of Engineering Mechanics and Energy, University of Tsukuba, Ibaraki, Japan
2. Graduate School, University of Tsukuba, Ibaraki, Japan
E-mail: isobe@kz.tsukuba.ac.jp

Received: 13 March 2025; Accepted: 27 April 2025; Available online: 10 May 2025

Abstract: In this study, numerical analyses of the displacements and axial forces of wall ties of a construction scaffolding under wind loads calculated based on fluid analysis and Safety Technical Guidelines of Scaffoldings were conducted. The OpenFOAM software, which is an open-source numerical solver based on the finite volume method, was used for the fluid analysis. The ASI–Gauss code, which is a finite element code using beam elements that can stably calculate nonlinear phenomena such as member fracture, was employed as the structural analysis code. The one-way fluid–structure coupled analysis revealed that the wind loads from one side of the building obtained using the fluid analysis are complex owing to flow separation and instantaneous flow. These loads may lead to very dangerous situations for the scaffolding, even if it is safe under the wind loads obtained using the Safety Technical Guidelines. Therefore, it is necessary to reinforce the middle and lower layers of the scaffolding, which are affected by the flow separation.
Keywords: Construction scaffoldings; Wind load; One-way coupled analysis; OpenFOAM; Fluid analysis; Structural analysis; ASI–Gauss code.

1. Introduction

Construction scaffoldings are used in many construction and demolition sites to facilitate work near buildings because of their high strength, durability, and ease of assembly and disassembly. However, one of the most common occupational hazards associated with scaffoldings is their collapse in strong winds. Scaffoldings are often equipped with protective sheets and soundproofing panels to prevent flying debris and construction noise. These sheets increase the area subjected to wind pressure, and strong winds have occasionally caused scaffoldings to collapse (Fig. 1) [1]. These collapsed scaffoldings can overhang roads and adjacent buildings, causing extensive damage to nearby facilities, pedestrians, and traffic networks. As these scaffoldings are prone to failure and can constitute a hazard to both their users and other people in the vicinity during work, interdisciplinary research on scaffolds has been conducted worldwide for over the past three decades, to determine the errors in the functioning of scaffolds, and to develop methods for increasing the safety of their usage [2–6].

To determine the safe load-carrying capacity of scaffoldings, Weesner and Jones [7] conducted load tests on four different types of frame scaffolding systems and predicted the ultimate load-carrying capacity of each system using both eigen buckling and geometrically nonlinear analyses. Takanashi *et al*. [8] showed that the pullout

Figure 1. Accidental collapse of scaffoldings due to strong winds occurred in Tokyo on March 2nd, 2021[1].

strength of the wall ties that connect scaffoldings to the walls of buildings is significantly lower than the tensile and compressive strengths of the wall ties themselves. Wang *et al*. [9] developed a probability-based design criteria for support scaffolding systems using a direct design method and revealed the variations in material and stiffness properties, as well as the model uncertainty of the advanced analysis in typical steel scaffolding structures under static loading. Lipecki *et al*. [10] analyzed the scaffolding responses to static wind action based on both the Eurocode standard and in-situ measurements. It was pointed out that during their operational use, scaffoldings could experience loads other than perpendicular or parallel to their façade as given in Eurocode. Recently, numerous research programs have demonstrated that nonlinear finite element methods can simulate the behavior and capture all relevant limit states of steel scaffolding structures, incorporating material and geometric nonlinearities, initial geometric imperfections, and semi-rigid joint stiffness [11–15]. For example, Błazik-Borowa *et al*. [15] presented a method of determining the probability of scaffolding failure at maximum loads by considering their geometric imperfections, condition of the anchors, and load-bearing capacity of the ground.

Most of the numerical investigations conducted in the above recent studies are based on static loadings, and although the Safety Technical Guidelines of Scaffoldings against Wind Loads [16] have been provided in Japan, the safety of scaffoldings against complex, dynamic flows, such as flow separation and instantaneous flow that occur around structures, has not been fully investigated. Understanding the wind loads acting on scaffoldings in such cases is extremely important for improving the safety of scaffoldings and their surroundings.

On the other hand, recent advances in fluid analysis technology have made it possible to evaluate wind loads acting on structures with a high degree of accuracy. Fluid analysis can simultaneously evaluate wind flow around a structure and the generated loads. Although fluid analysis has been applied to a single or group of buildings, there are no previous studies concerning scaffoldings attached to those buildings under dynamic loads. The main aim of this study is to conduct fluid analysis on a scaffolding attached to a building to calculate the dynamic wind flow around the scaffolding and wind-generated dynamic loads acting on the scaffolding. In addition, one-way fluid–structure coupled analysis was performed on the structural analysis model of the scaffolding to compare its behaviors under those wind loads obtained based on the fluid analysis and Safety Technical Guidelines. OpenFOAM [17], an open-source fluid analysis software, was used for the fluid analysis, and the adaptively shifted integration (ASI)–Gauss code [18] was applied for the structural analysis.

The specific procedures of this study are as follows:

1) A building with a five-story, four-span construction scaffolding was analyzed by applying wind inflows from three directions (front, rear, and side) to the model. In particular, the side case, in which the scaffolding was pulled away from the building, was investigated.

2) The wind flow and wind loads acting on the sheet surface of the construction scaffolding were evaluated based on the results of the fluid analysis.

3) The obtained wind loads were applied as external forces, and a structural analysis was performed using the ASI–Gauss code to evaluate the behavior of the construction scaffolding and axial forces acting on the wall ties.

4) The wind loads calculated from the fluid analysis were compared with those obtained from the Safety Technical Guidelines, along with the structural analysis results based on them.

The remainder of this paper is organized as follows. In Section 2, an overview on construction scaffoldings is presented and the calculation method of wind loads according to the Safety Technical Guidelines is explained. In Section 3, the numerical framework for fluid analysis is described. Section 4 discusses the numerical analysis of a construction scaffolding subjected to wind loads obtained using the fluid analysis in comparison with those obtained using the Safety Technical Guidelines. Finally, Section 5 summarizes the conclusions drawn from the results.

Figure 2. Photograph of a construction scaffolding.

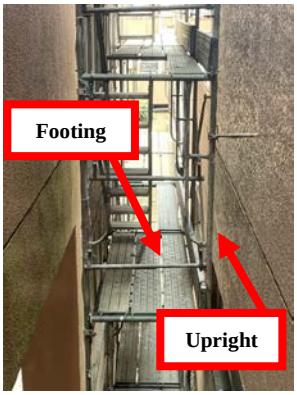

Figure 3. Uprights and footings.

Figure 4. Diagonal braces.

Figure 5. Wall ties.

2. Construction scaffoldings

2.1 Overview of construction scaffoldings

There are several types of scaffoldings used in construction and demolition sites in Japan. In this study, construction scaffoldings, which are commonly used at many construction sites because of their lightweight and ease of assembly, are the target of the analysis. Figure 2 shows a photograph of a Japanese standard construction scaffolding. Among the many components used in construction scaffoldings, the uprights and footings (Fig. 3), diagonal braces (Fig. 4), and wall ties (Fig. 5) significantly affect the strength of scaffoldings. The uprights are members that serve as columns in the scaffolding structure and are connected with footings, horizontal beams, and stiffeners to constitute a scaffold system. The dimensions of the scaffold system vary from 1600 to 2000 mm in height and 600 to 1219 mm in width. Scaffoldings with heights of 1700 mm and widths of 900–1200 mm are commonly used. The frame with a footing is passed between the frames to serve as a working floor. Its length is less than 1850 mm, its width is 240–500 mm, and the thickness of the footing material is 1.1 mm or greater. Diagonal braces are members used to reinforce scaffoldings and are available in two types: 1800 mm span with 1200 mm length, and 1829 mm span with 1219 mm length. Wall ties secure the scaffolding to the building wall and are driven into the exterior wall surface of the building via anchors.

2.2 Calculation method of wind loads according to the Safety Technical Guidelines

The Safety Technical Guidelines [16] provide a simple method for calculating the wind load acting on scaffoldings to ensure the safety of scaffoldings against wind loads. The wind load P acting on the scaffolding is calculated using the following equation:

$$P = C_i q_z A \tag{1}$$

where C_i, q_z, and A are the wind power coefficient, velocity pressure [N/m^2], and active area [m^2], respectively. The velocity pressure q_z is given by the following equation based on the air density ρ [kg/m^3] and wind speed U_z [m/s] at height z [m].

$$q_z = \frac{1}{2}\rho {U_z}^2 \tag{2}$$

where

Table 1. Correction factor based on the location of scaffoldings attached to a building [16].

Direction of wind loads	Location of sheets and nets	Correction factor
Positive (from front side)	Top two layers	1.0
	Other parts	1.31
Negative (from rear side)	Two spans from opening and protrusions	1.0
	Two spans from corner	0.77
	Other parts	0.62

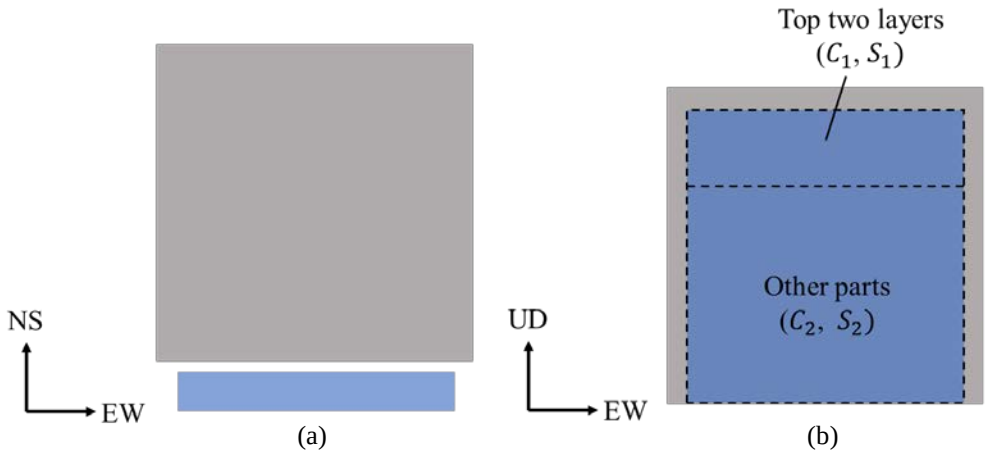

Figure 6. Wind power coefficients and areas depending on the scaffolding location when a wind load is acting from the front side of the scaffolding; (a) Plan view; (b) Front view.

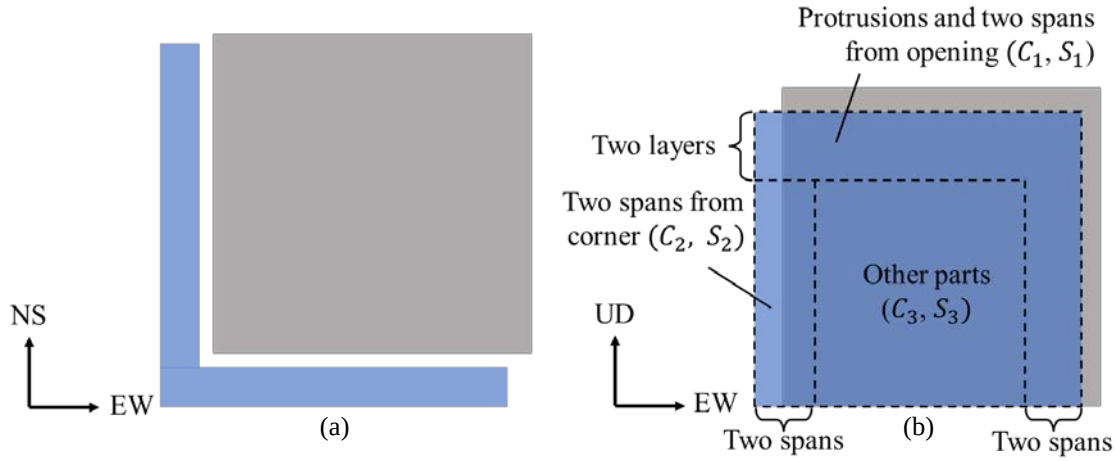

Figure 7. Wind power coefficients and areas depending on the scaffolding location when wind loads are acting from the rear side of the scaffolding and the scaffoldings are placed at two or more sides of the building; (a) Plan view; (b) Front view.

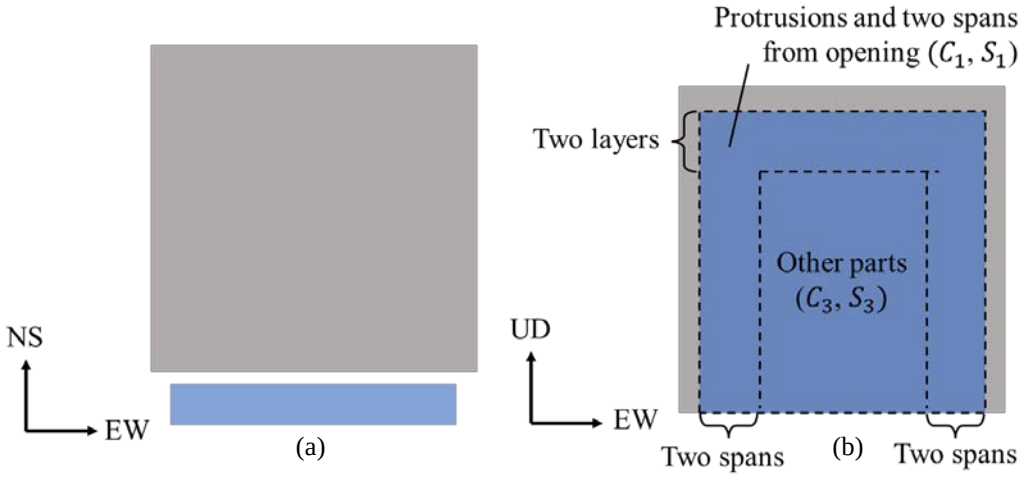

Figure 8. Wind power coefficients and areas depending on the scaffolding location when wind loads are acting from the rear side of the scaffolding and the scaffoldings are placed only at one side of the building; (a) Plan view; (b) Front view.

$$U_z = U_0 \left(\frac{z}{z_0}\right)^{\alpha} \tag{3}$$

and z_0, U_0, and α are the reference height [m], wind speed at the reference height [m/s], and power exponent that represents the vertical distribution of wind speed, respectively.

The wind power coefficient C_i is determined using the average wind power coefficient $\bar{C}$ obtained from wind tunnel test results and a correction factor based on the location of the scaffolding attached to the building. The correction factor depends on the direction of the wind load and location of sheets and nets, as presented in Table 1 [16]. In the case of a positive wind load, i.e., a wind load acting from the front side of the scaffolding, the following relationship is obtained using the correction factor, wind power coefficient C_1 and area of top two layers S_1, and those of other parts (C_2 and S_2), as shown in Fig. 6.

$$\frac{1}{S_1+S_2}(S_1C_1 + S_2C_2) = \bar{C} \tag{4}$$

$$C_2 = 1.31C_1 \tag{5}$$

In the case of negative wind loads, i.e., wind loads acting from the rear side of the scaffolding, corner parts should be considered if the scaffoldings are placed at two or more sides of the building, as depicted in Fig. 7. The following relationship is obtained using the wind power coefficient C_1 and area of protrusions and two spans from the opening S_1, wind power coefficient C_2 and area of two spans from the corner S_2, and those of other parts (C_3 and S_3).

$$\frac{1}{S_1+S_2+S_3}(S_1C_1 + S_2C_2 + S_3C_3) = \bar{C} \tag{6}$$

$$C_2 = 0.77C_1 \tag{7}$$

$$C_3 = 0.62C_1 \tag{8}$$

If the scaffoldings are placed only at one side of the building, as displayed in Fig. 8, both C_2 and S_2 are zero because there is no corner part. Solving Eqs. (6)–(8) yields the wind power coefficient under negative wind loads. Using the average wind power coefficients obtained from wind tunnel experiments [16] (Table 2) and the above equations, the wind power coefficient for the five-story, four-span scaffolding considered in this study can be calculated as shown in Fig. 9.

As described above, the wind load calculation in the Safety Technical Guidelines is based on the velocity pressure, wind power coefficient, and active area. However, the guidelines do not consider complex and dynamic flows such as flow separation and instantaneous flow that occur around structures. In particular, scaffoldings on buildings are susceptible to flow separation when wind flows in from the side of the structure, making it almost impossible to estimate the expected wind loads.

Table 2. Average wind power coefficients for the entire scaffolding obtained from wind tunnel experiments [16].

Inflow direction	Front side of structure	Rear side of structure	Side of structure
Average wind power coefficient $\bar{C}$	1.47	-0.10	-0.25

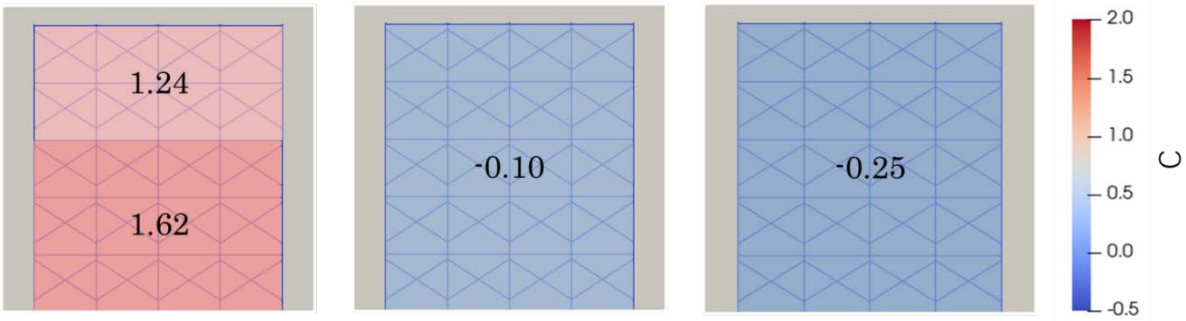

(a) (b) (c)

Figure 9. Calculated wind power coefficients for a five-story, four-span scaffolding; (a) Inflow from the front side; (b) Inflow from the rear side; (c) Inflow from the side.

3. Numerical framework for fluid analysis

This section describes the theory applied to OpenFOAM, which is used in the fluid analysis.

3.1 Governing equations

The equation of continuity for an incompressible fluid is expressed as

$$\nabla \cdot \boldsymbol{u} = 0 \tag{9}$$

where $\boldsymbol{u}$ is the velocity. The Navier–Stokes equation is given by

$$\frac{\partial \boldsymbol{u}}{\partial t} + (\boldsymbol{u} \cdot \boldsymbol{\nabla})\boldsymbol{u} = -\frac{1}{\rho}\nabla p + \nu \nabla^2 \boldsymbol{u} + \boldsymbol{f} \tag{10}$$

where ρ, ν, and $\boldsymbol{f}$ are the density, kinematic viscosity, and external force on the fluid, respectively.

3.2 Time integration scheme

The Euler implicit scheme is used for discretization in the time direction. If time is divided into a finite number of steps and the time derivative is expressed in differential form, Eq. (10) at $n+1$ step can be written as follows:

$$\frac{\boldsymbol{u}^{n+1} - \boldsymbol{u}^{n}}{\Delta t} = -(\boldsymbol{u}^{n+1} \cdot \boldsymbol{\nabla})\boldsymbol{u}^{n+1} - \frac{1}{\rho}\nabla p^{n+1} + \nu \nabla^2 \boldsymbol{u}^{n+1} + \boldsymbol{f}^{n+1} \tag{11}$$

3.3 Spatial integration scheme using the finite volume method

The finite volume method is used for discretization in the spatial direction [19]. In the finite volume method, a continuum is divided into hexahedrons of arbitrary shapes (hereinafter referred to as "cells"), and the equations are expressed as volume integrals for each cell. In the following, P, N, and f are the center point of the cell of interest, center point of the adjacent cell, and center point of the boundary plane between the cell of interest and adjacent cell, respectively.

The transport equation for the physical quantity ϕ is expressed as

$$\frac{\partial \rho \phi}{\partial t} + \nabla \cdot (\rho \phi \boldsymbol{u}) = \nabla \cdot (k \nabla \phi) + s \tag{12}$$

where k and s are the diffusion coefficient and source term, respectively. Volume integration of Eq. (12) over the cell area yields the following equation:

$$\int_V \frac{\partial \rho \phi}{\partial t} dV + \int_V \nabla \cdot (\rho \phi \boldsymbol{u}) dV = \int_V \nabla \cdot (k \nabla \phi) dV + \int_V s dV \tag{13}$$

If ρ, ϕ, and s are constant in the cell, then the first term on the left side and the second term on the right side of Eq. (13) can be written as

$$\int_V \frac{\partial \rho \phi}{\partial t} dV = \frac{\partial \rho_P \phi_P}{\partial t} V_P \tag{14}$$

$$\int_V s dV = s_P V_P \tag{15}$$

By applying Gauss's divergence theorem to the second term on the left side and the first term on the right side of Eq. (13), the expressions become

$$\int_V \nabla \cdot (\rho \phi \boldsymbol{u}) dV = \int_S (\rho \phi \boldsymbol{u}) \cdot \boldsymbol{n} dS \approx \sum_f \rho \phi_f \boldsymbol{u}_f \cdot \boldsymbol{S}_f \tag{16}$$

$$\int_V \nabla \cdot (k \nabla \phi) dV = \int_S (k \nabla \phi) \cdot \boldsymbol{n} dS \approx \sum_f k_f (\nabla \phi)_f \cdot \boldsymbol{S}_f \tag{17}$$

where $\boldsymbol{n}$ is the normal vector of the cell surface, and $\boldsymbol{S}_f$ is a vector perpendicular to the cell boundary surface and having the area of the cell boundary surface as its size. Note that ϕ and $\boldsymbol{u}$ are assumed constant within the cell boundary plane.

Because the value of ϕ_f at the center of the boundary plane between the cell of interest and adjacent cell is unknown, ϕ_f is interpolated as follows by applying the central difference method to ϕ_P and ϕ_N at the center points of the cells.

$$\phi_f = w\phi_P + (1-w)\phi_N \tag{18a}$$

$$w = \frac{|\boldsymbol{x}_f - \boldsymbol{x}_N|}{|\boldsymbol{x}_N - \boldsymbol{x}_P|} \tag{18b}$$

where w is the weight and $\boldsymbol{x}_P$, $\boldsymbol{x}_N$, and $\boldsymbol{x}_f$ are the position vectors of the respective center points. The gradient $(\nabla\phi)_f$ is interpolated as the gradient normal to the boundary surface in the form $(\nabla\phi)_f \cdot \boldsymbol{S}_f$ as follows:

$$(\nabla\phi)_f \cdot \boldsymbol{S}_f = \frac{\phi_N - \phi_P}{|\boldsymbol{x}_N - \boldsymbol{x}_P|}|\boldsymbol{S}_f| \tag{19}$$

Substituting Eqs. (14)–(19) into Eq. (13) yields the following:

$$\frac{\partial \rho_P \phi_P}{\partial t} V_P + \sum_f \rho \phi_f \boldsymbol{u}_f \cdot \boldsymbol{S}_f = \sum_f k_f \frac{\phi_N - \phi_P}{|\boldsymbol{x}_N - \boldsymbol{x}_P|}|\boldsymbol{S}_f| + s_P V_P \tag{20}$$

In general, Eq. (20) is written in the form of an algebraic expression as follows:

$$A_P \phi_P + \sum A_N \phi_N = b \tag{21}$$

Extending Eq. (21) to the entire system, we obtain a simultaneous linear equation consisting of a coefficient matrix with A_P and A_N as components, an unknown vector with ϕ_P and ϕ_N as components, and a right side vector with b as a component.

3.4 Pressure–velocity coupling

Equation (10) can be discretized by the finite volume method as follows:

$$A_P \boldsymbol{u}_P + \sum A_N \boldsymbol{u}_N = -\nabla p + \boldsymbol{s}_P \tag{22}$$

where $\boldsymbol{s}_P$ is a source term other than the pressure term. Solving this equation for $\boldsymbol{u}_P$ yields

$$\boldsymbol{u}_P = \frac{\boldsymbol{s}_P - \sum A_N \boldsymbol{u}_N}{A_P} - \frac{1}{A_P}\nabla p \tag{23}$$

Substituting the above equation into Eq. (9), we obtain the following pressure equation:

$$\nabla \cdot \left(\frac{1}{A_P}\nabla p\right) = \nabla \cdot \left(\frac{\boldsymbol{s}_P - \sum A_N \boldsymbol{u}_N}{A_P}\right) \tag{24}$$

Substituting the pressure obtained by solving Eq. (24) into Eq. (23) yields the velocity.

3.5 Turbulent flow model

To deal with turbulent phenomena, the RNG k-ε model [20] is used in this study. In this model, the model constants are derived theoretically, and it can predict complex flows better than the standard k-ε model. The transport equation for turbulent energy k is expressed as

$$\frac{\partial k}{\partial t} + \frac{\partial k \bar{u}_j}{\partial x_j} = P_k - \varepsilon + D_k \tag{25}$$

where P_k and D_k are the generation and diffusion terms of turbulence energy, respectively. The transport equation for the turbulent dissipation rate ε is given by

$$\frac{\partial \varepsilon}{\partial t} + \frac{\partial \varepsilon \bar{u}_j}{\partial x_j} = \frac{\varepsilon}{k}(C_{\varepsilon 1}{}^* P_k - C_{\varepsilon 2}\varepsilon) + D_\varepsilon \tag{26a}$$

$$C_{\varepsilon 1}{}^* = C_{\varepsilon 1} - \frac{\eta(1-\eta/\eta_0)}{1+\alpha\eta^3} \tag{26b}$$

$$\eta = \frac{k}{\varepsilon}\sqrt{2\bar{D}_{ij}\bar{D}_{ij}} \tag{26c}$$

where D_ε is the diffusion term of the turbulent dissipation rate, η is the similarity variable, and $C_{\varepsilon 1}$ and $C_{\varepsilon 2}$ are the model constants. $C_{\varepsilon 1}$ is corrected from the standard k-ε model. The model constants in the RNG k-ε model are as follows:

$$C_\mu = 0.0845,\quad C_{\varepsilon 1} = 1.42,\quad C_{\varepsilon 2} = 1.68,\quad \eta_0 = 4.38,\quad \alpha = 0.012 \tag{27}$$

The above model can be used to reproduce complex flows with separation and large curvature.

3.6 Simulation of a wind tunnel experiment

Using the turbulence model described in the previous section, we attempted to reproduce the result of a wind tunnel experiment [21]. In the experiment, the ambient airflow was measured by particle image velocimetry and the wall pressure of a cube model of 115 mm per side was obtained using a multi-point wind pressure measurement device. The average wind speed at the top of the cube was approximately 10 m/s and the turbulent energy was approximately 0.5 m^2/s^2. The sampling frequency was 1000 Hz and the sampling time was 8.192 s.

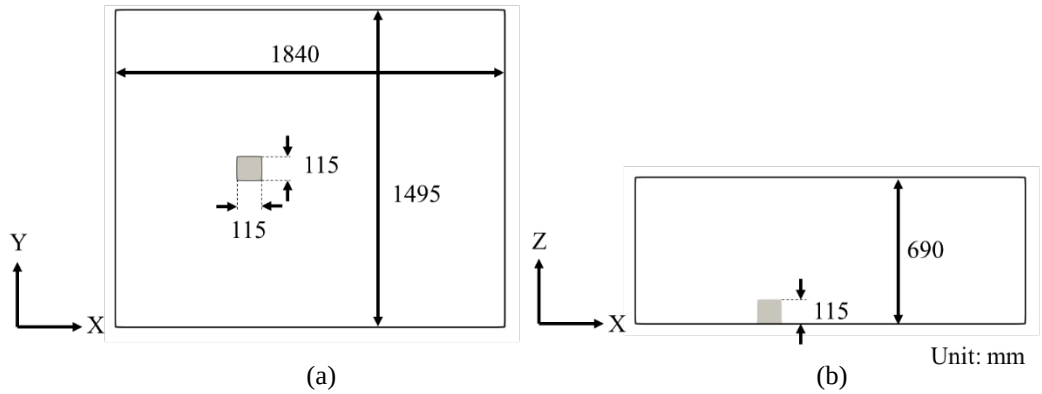

(a) (b)

Figure 10. Numerical model for a simulation of a wind tunnel experiment; (a) Plan view; (b) Front view.

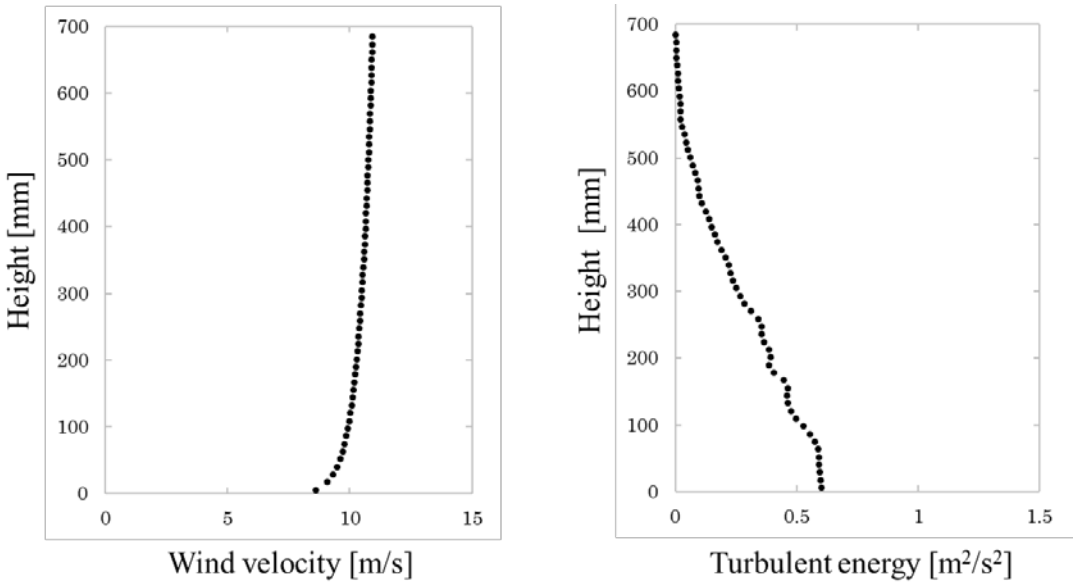

(a) (b)

Figure 11. Vertical distribution of incoming airflow applied in the fluid analysis; (a) Vertical distribution of wind velocity; (b) Vertical distribution of turbulent energy.

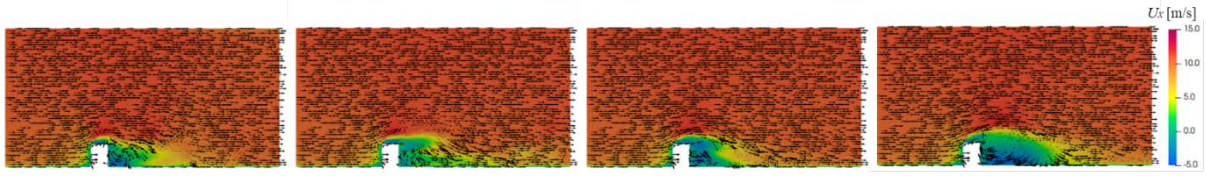

(a) (b) (c) (d)

Figure 12. X-axis component of wind velocity at the cutting plane shown in Fig. 13; (a) $t = 1.0$ s; (b) $t = 2.0$ s; (c) $t = 4.0$ s; (d) $t = 8.0$ s.

The numerical model is depicted in Fig. 10. The analysis domain is a rectangular space with dimensions of 1840 mm × 1495 mm × 690 mm. The cube is 115 mm on a side, as in the experiment. The non-slip condition was applied to the ground and cube surfaces, and the symmetry condition was applied to the sides and top of the analysis domain. As in the experiment, air is flowed in toward the positive X-axis direction with the velocity and turbulence energy displayed in Fig. 11. The RNG k-ε model described in the previous section was used as the turbulence model. The time increment was 0.001 s and the total analysis time was 8.192 s, the same as in the experiment.

Figure 12 illustrates the distribution of the X-axis component of the wind velocity in the plane when the numerical model is cut as shown in Fig. 13. The black arrows in the figure indicate the wind direction in the plane. From the figure, the flow separation becomes more pronounced on the upper surface of the cube with time. Figures 14(a) and 14(b) display the wind power coefficient distribution when the location on the wall is defined as shown in the figure and the average wind power coefficient obtained from the wind tunnel experiments [21], respectively. The wind power coefficients from both results agree well with each other, indicating that the turbulence model used in the fluid analysis is appropriate.

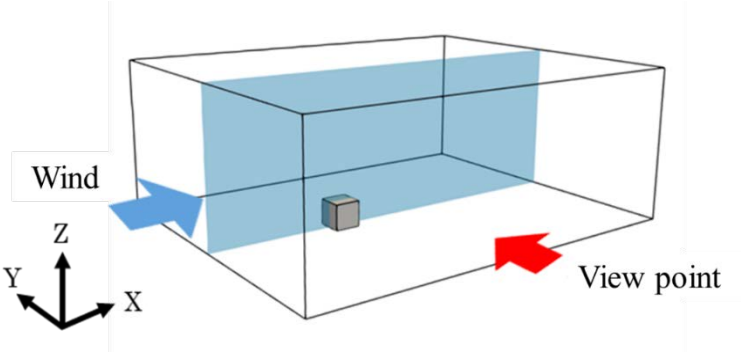

Figure 13. Cutting plane in the model.

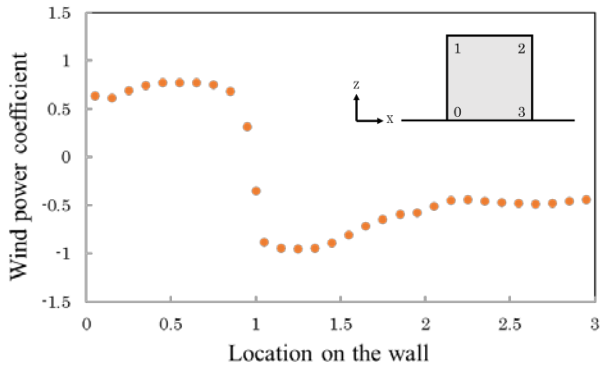

(a)

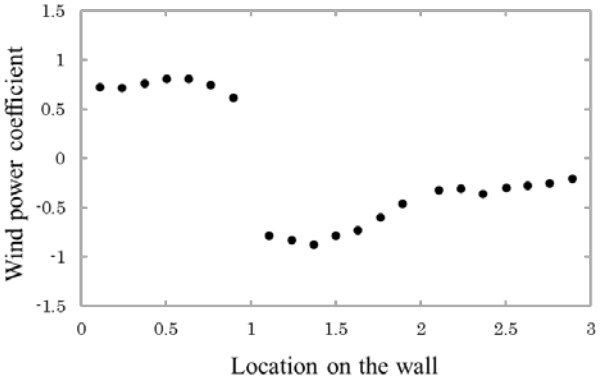

(b)

Figure 14. Comparison between numerical and wind tunnel experiment results**;** (a) Wind power coefficients obtained from fluid analysis at t = 1.0 s; (b) Average wind power coefficients obtained from wind tunnel experiments.

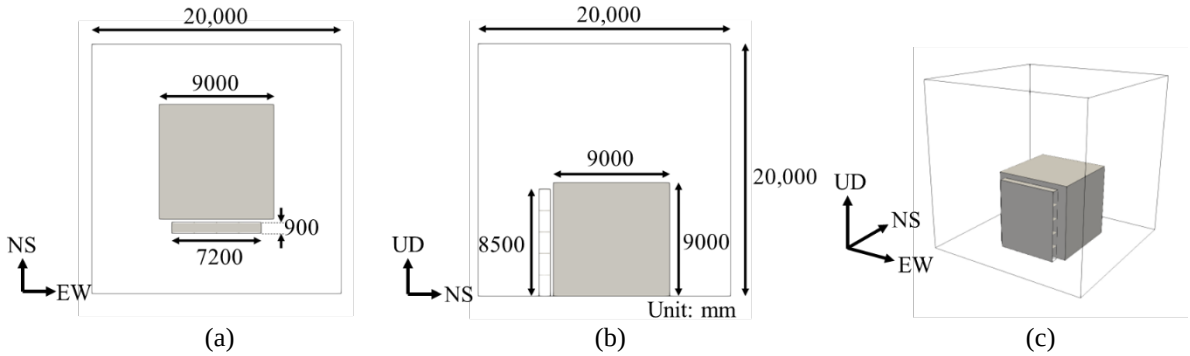

Figure 15. Numerical model for fluid analysis; (a) Plan view; (b) Side view; (c) Isometric view.

4. Numerical analysis of a construction scaffolding under wind loads

4.1 Numerical model

A fluid analysis of an area around a construction scaffolding was conducted using the numerical method described in the previous section. A diagram of the fluid analysis model is depicted in Fig. 15. The analysis domain is a cube with 20,000 mm sides. A cube of 9000 mm per side is assumed as a building, and a five-story, four-span scaffolding is installed in front of the building with a clearance of 250 mm to the building. The dimensions of the scaffolding are 8500 mm high, 7200 mm wide, and 900 mm deep. For simplicity, the cross-sections of the footings and diagonal braces of the scaffolding are squares, 48.6 mm on a side. The sheet attached to the front of the scaffolding is assumed to be void-free, with a thickness of 2 mm. The total number of cells is 37,648,304.

The schematic and detail of the structural analysis model are shown in Figs. 16 and 17, respectively. The dimensions of the scaffolding are 8500 mm high, 7200 mm wide, and 900 mm deep, as in the fluid analysis model. The connections between uprights and horizontal beams, between uprights and diagonal braces, and between uprights and wall ties were pin-jointed. The mass of the footing was set to 25 kg and was considered by adjusting the density of the members. The locations of the structural nodes subjected to wind loads are illustrated in Fig. 18. For convenience, the structural nodes, where wind loads are applied, are numbered from the lower left to the upper right as "0-0, 0-1, ..., 5-3, 5-4." Ten wall ties were attached to each layer at both ends of the scaffolding, as shown in Fig. 19. The numberings of the wall ties are the same as those of the structural nodes subjected to wind loads. The installation spacing is within five layers in the layer direction and four spans in the span direction, as specified

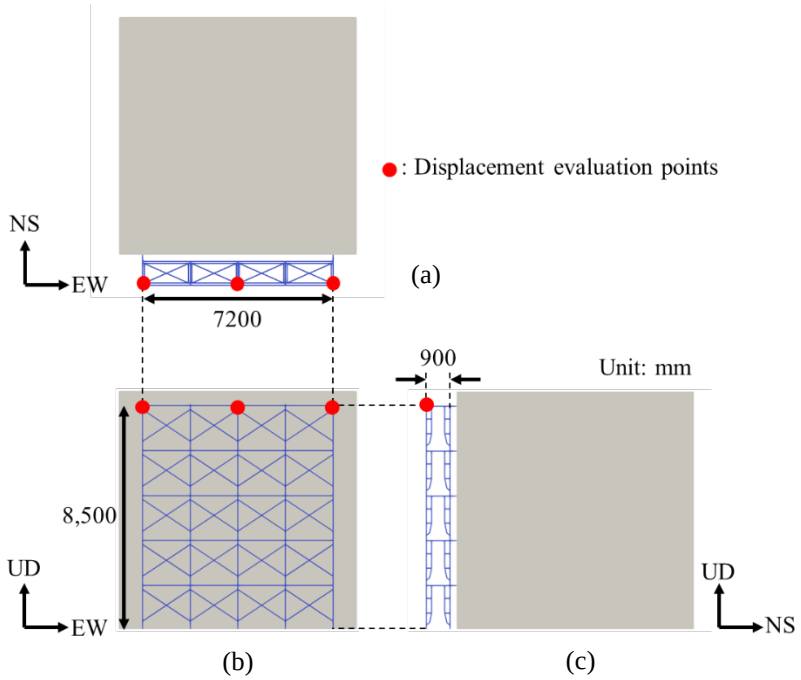

Figure 16. Numerical model for structural analysis; (a) Plan view; (b) Front view; (c) Side view.

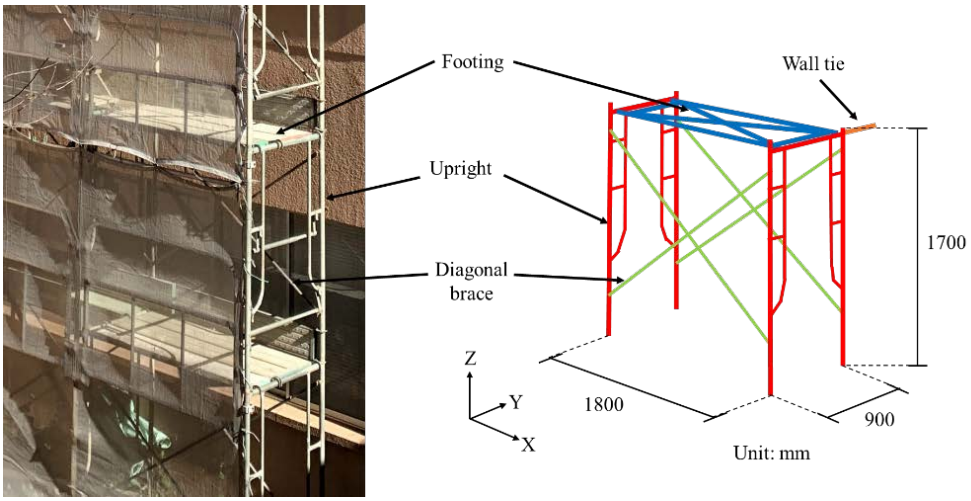

Figure 17. Detail of the structural analysis model.

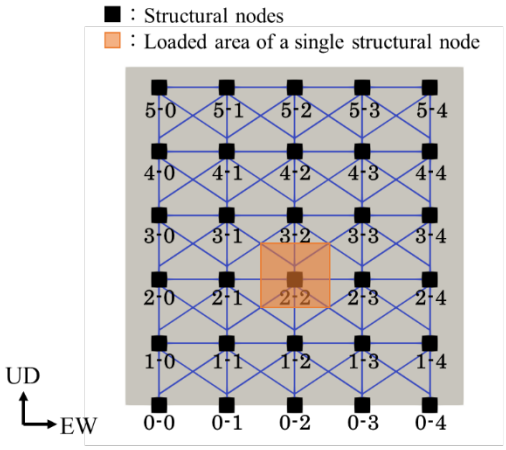

Figure 18. Locations of structural nodes subjected to wind loads.

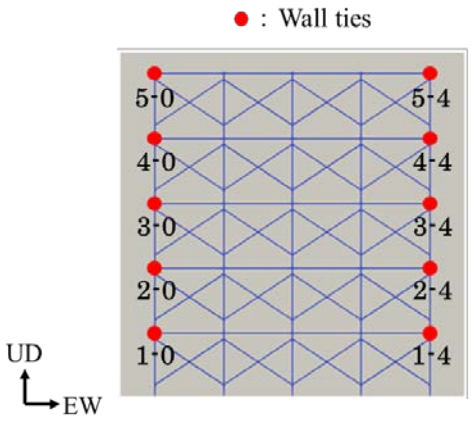

Figure 19. Attached positions of wall ties.

by the Occupational Safety and Health Regulations [22]. To simulate pull out of the wall ties from the exterior wall surface, the element was fractured by applying a tensile axial force of 2000 N or over on the wall ties [8]. To simulate pullout between uprights, a small element between frames was fractured by applying a tensile axial force of 9807 N or over on the element [23]. The sheet was not modeled in the structural analysis, but only its weight was considered by setting its mass per unit area to 1.2 kg/m^2 and adding it as density to the members on the side to which the sheet was attached. All the bottoms of the lowest frames were pin-jointed, and the wall ties were fully restrained.

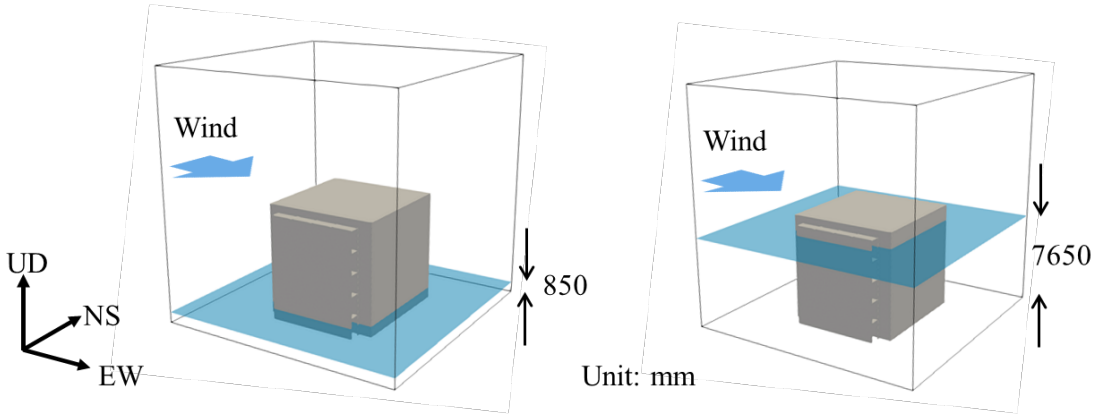

Figure 20. Wind inflow direction and cutting planes of the numerical model.

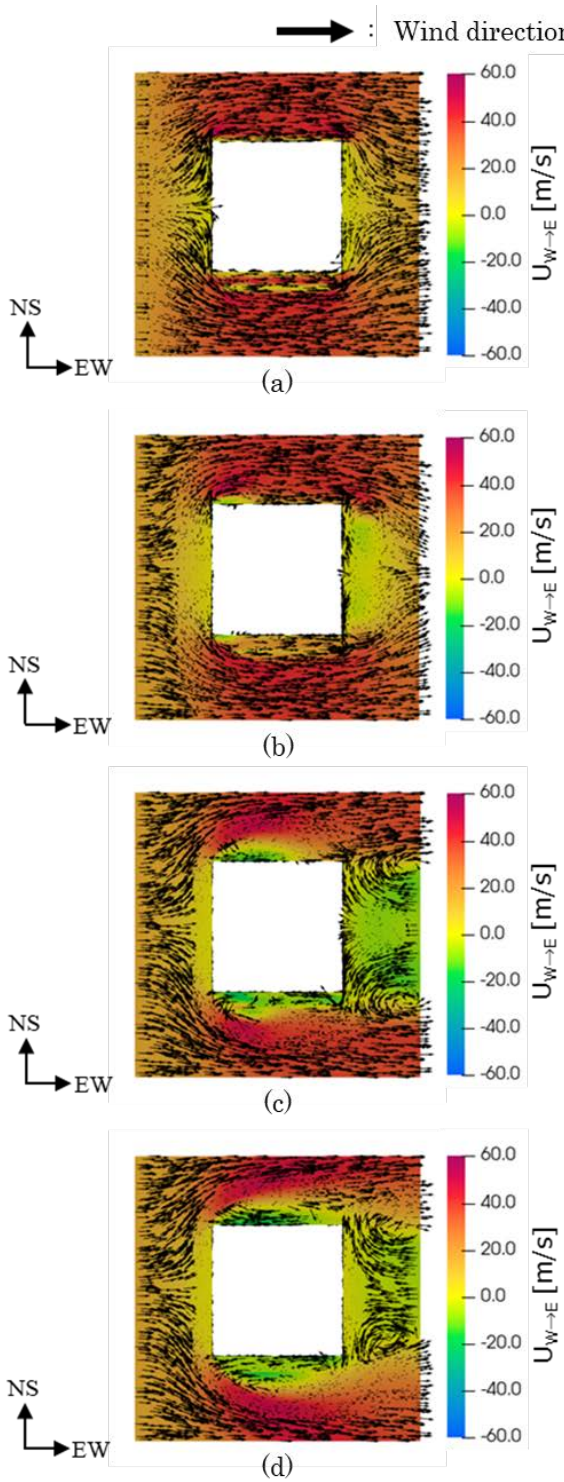

Figure 21. Wind velocity distribution in the cutting plane at height of 850 mm; (a) $t = 0.1$ s; (b) $t = 1.0$ s; (c) $t = 4.0$ s; (d) $t = 8.0$ s.

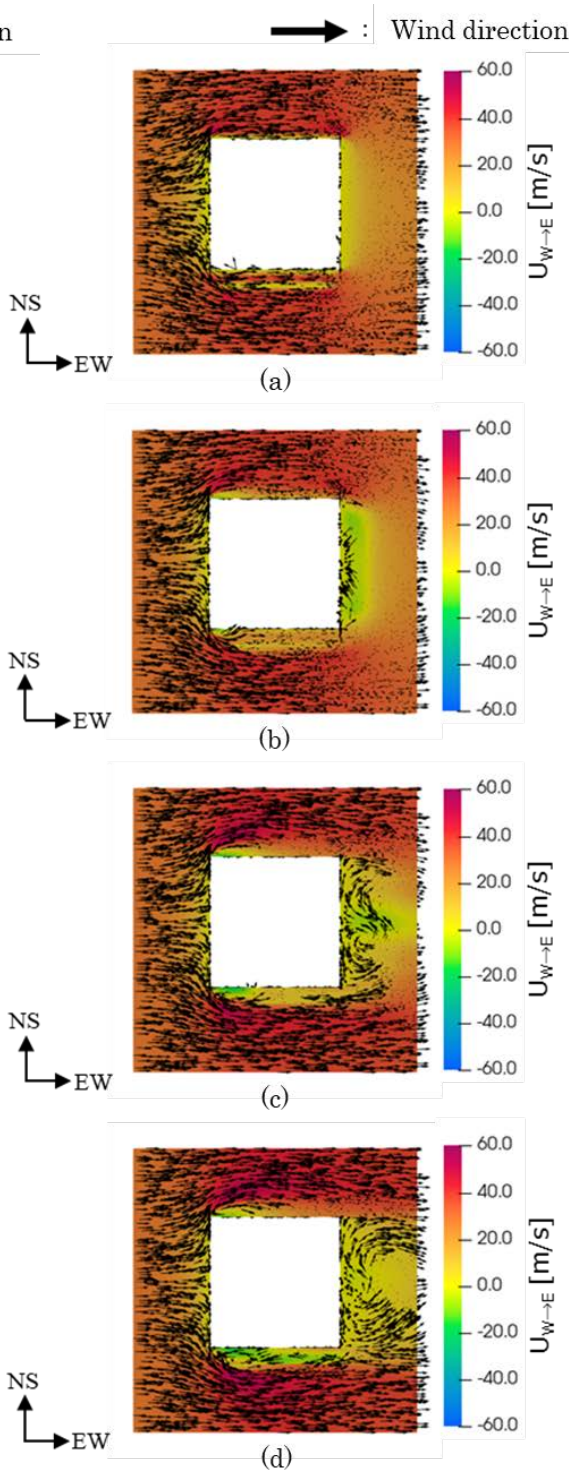

Figure 22. Wind velocity distribution in the cutting plane at height of 7650 mm; (a) $t = 0.1$ s; (b) $t = 1.0$ s; (c) $t = 4.0$ s; (d) $t = 8.0$ s.

4.2 Numerical conditions

For the boundary conditions in the fluid analysis, no-slip condition was applied to the ground and structure surfaces, and the symmetry condition was applied to the sides and top of the analysis domain. For the inflow condition, U_z is given according to Eq. (3), considering that the wind velocity is distributed in the height direction.

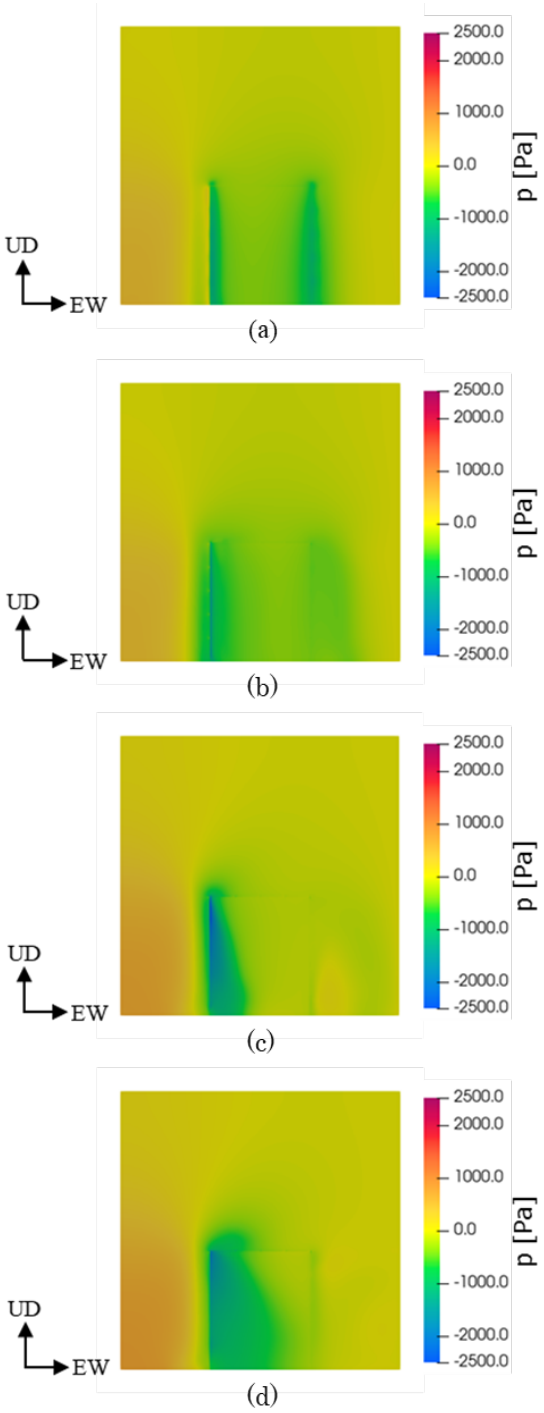

Figure 23. Pressure distribution at front side of the sheet; (a) $t = 0.1$ s; (b) $t = 1.0$ s; (c) $t = 4.0$ s; (d) $t = 8.0$ s.

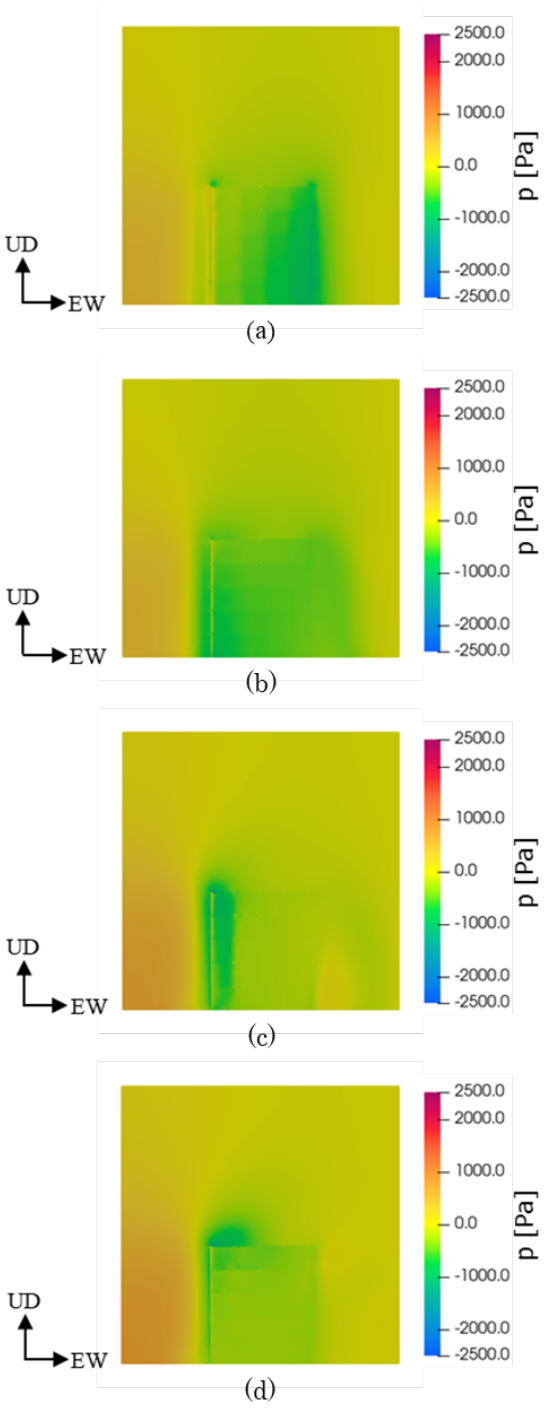

Figure 24. Pressure distribution at rear side of the sheet; (a) $t = 0.1$ s; (b) $t = 1.0$ s; (c) $t = 4.0$ s; (d) $t = 8.0$ s.

In this analysis, z_0 = 10 m and U_0 = 30 m/s, and the power exponent was set to α = 0.27 by assuming a region dominated by medium-rise buildings of 4 to 9 stories.

Because the wind loads did not act in the direction of the scaffoldings being pulled away from the building when wind flowed in from the front and rear sides, we focused on the case where wind flowed in from the side of the structure, as depicted in Fig. 20. The RNG k-ε model was used as the turbulence model, and the analysis was performed for 8 s with a time increment of 0.001 s. Based on the pressure p_i at fluid node i obtained from the fluid analysis, the wind load F_j acting on structural node j was calculated, and the time-history waveform of the wind

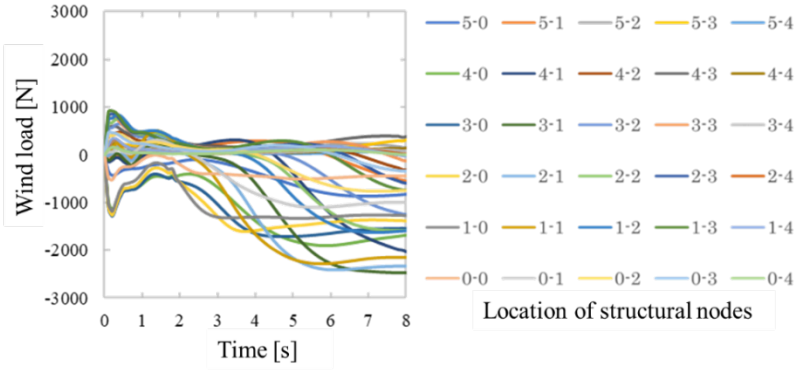

Figure 25. Time-history waveforms of wind loads calculated based on fluid analysis.

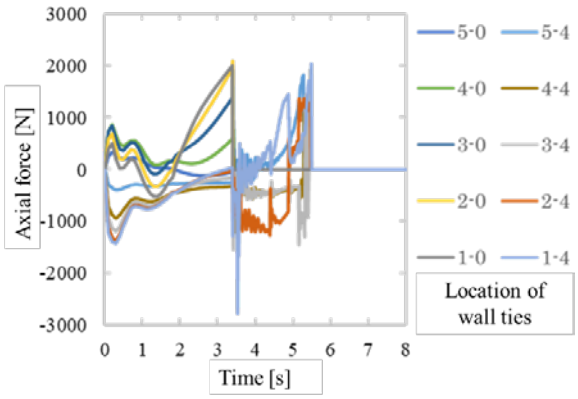

Figure 26. Axial forces acting on the wall ties under wind loads calculated based on fluid analysis.

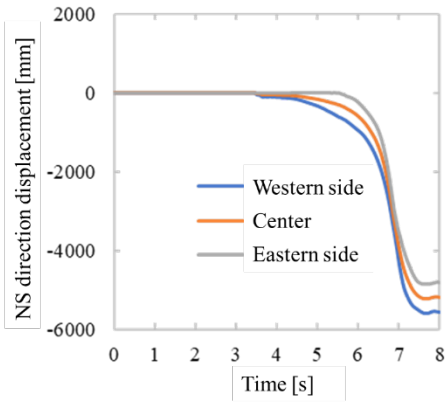

Figure 27. NS direction displacements at the top of the scaffolding under wind loads calculated based on fluid analysis.

load was created as input to the structural analysis. The wind load F_j acting on structural node j is calculated using the following equation:

$$F_j = \int_{A_i} p\, dA \approx p_1 A_1 + \cdots + p_{n_i} A_{n_i} = \frac{A_j}{n_j} \sum_{i=1}^{n_j} p_i \tag{28}$$

where A_j and n_j are the loaded area of structural node j and total number of fluid nodes i in A_j, respectively. For the structural analysis, a time increment of 0.001 s was also used, and the analysis was performed for 8 s.

4.3 Numerical results

The wind velocity distributions in the cutting planes described in Fig. 20 are displayed in Figs. 21 and 22. As shown in these figures, wind flows in between the scaffolding and building immediately after the beginning of the analysis, before the occurrence of flow separation. Flow separation then occurs from the upwind side of the

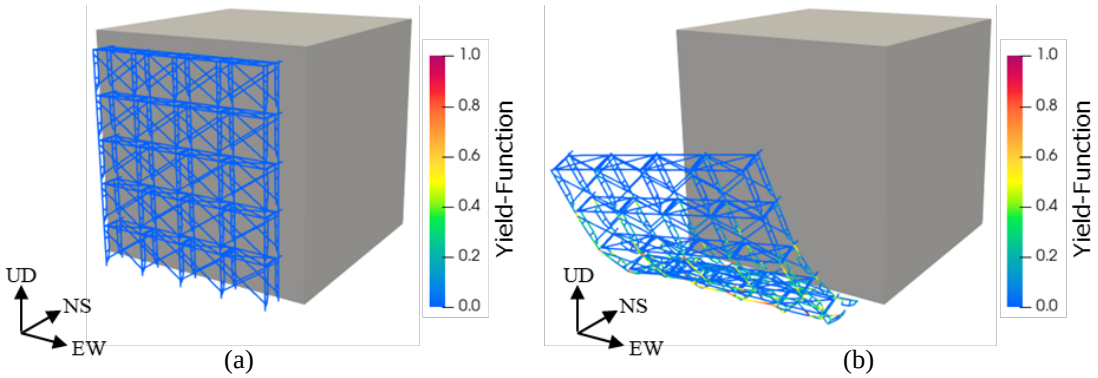

Figure 28. Structural analysis result; (a) Initial stage; (b) Final stage. The wall ties were pulled out in the order of layers 1, 2, 3, 4, and 5 at approximately 3.5 s.

building and scaffolding and spreads to the downwind side with time. The flow separation is more significant in the middle and lower layers than in the upper layers, and the separation area is wider. The pressure distributions at the front and rear sides of the sheet are depicted in Figs. 23 and 24. Figure 23 shows that the pressure at the front side of the sheet becomes negative from upwind to downwind with time. The range of negative pressure is larger in the middle and lower layers than in the upper layers; this is because the separation area is wider in the middle and lower layers. In contrast, Fig. 24 shows that the pressure at the rear side of the sheet becomes negative immediately after the beginning of the analysis owing to vortex generation on the upwind side, and the pressure gradually stabilizes as the vortex disappears with time.

The time-history waveforms of the wind loads obtained by inputting the results of the fluid analysis into Eq. (28) are illustrated in Fig. 25. The axial forces acting on the wall ties and the NS displacements at the top of the scaffolding when the waveforms are applied as input in the structural analysis, are depicted in Figs. 26 and 27, respectively. From 2.0 s onward, the axial forces on the wall ties attached to layers 1 to 3 on the windward side became particularly large, and the wall ties were pulled out eventually, in the order of layers 1, 2, 3, 4, and 5 at approximately 3.5 s. This was because the separation area was wider below the middle layer of the scaffolding, and the wind load increased in the direction that the scaffolding was pulled away from the building. Later, at approximately 5.0 s, the wall ties on the downwind side were also pulled out, leading to the collapse of the scaffolding, as illustrated in Fig. 28, creating a very dangerous situation. Thus, when the scaffolding is greatly affected by flow separation, the wall ties may be pulled out from the middle layer of the scaffolding or below. In the five-story, four-span scaffolding analyzed in this study, for example, it is necessary to reinforce the third and lower layers.

For comparison, the time-history waveforms of the wind loads calculated based on the Safety Technical Guidelines, axial forces acting on the wall ties, and NS displacements of the top of the scaffolding when those wind loads are applied, are shown in Figs. 29, 30, and 31, respectively. The trends of the wind loads calculated using the fluid analysis (Fig. 25) and those calculated based on the Safety Technical Guidelines (Fig. 29) are significantly different. The wind loads calculated by the fluid analysis are very complicated owing to the occurrence of flow separation and instantaneous flow generated between the scaffolding and building. However, the Safety Technical Guidelines do not take such complex flows into account at all, and the resulting wind loads are not high enough to pull out the wall ties. Thus, we should always recognize that the Safety Technical Guidelines cannot cope with sudden changes in flow, such as at the beginning of a windstorm, or with the ever-changing pressure distribution caused by the occurrence of flow separation. We can observe from Fig. 25 that the maximum wind load can become approximately 1.6 times larger than the wind load when the wall ties are pulled out at 3.5 s. Thus, the anchors for the wall ties may need at least 160% reinforcement to overcome those effects if the number of wall ties remains the same. Or, to achieve the same result, the number of wall ties should be increased to at least 160% of the original number if the strength of the wall ties remains the same, and they should be used to reinforce the middle and lower layers of the scaffoldings. Extra six wall ties, in the case of a five-story, four-span construction scaffolding, could be installed at the first and second layer.

5. Conclusions

In this study, considering the case of a five-story, four-span construction scaffolding installed on one side of a building, a fluid analysis was conducted using the OpenFoam software to calculate the wind loads acting on the scaffolding when the wind flowed in from one side of the building. The obtained wind loads were applied as external forces, and structural analysis was conducted using the ASI–Gauss code to investigate the behavior of the scaffolding. Following are the main findings:

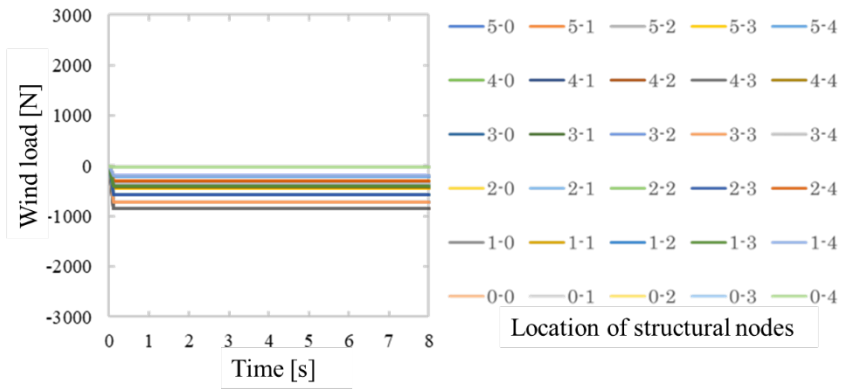

Figure 29. Time-history waveforms of wind loads calculated based on the Safety Technical Guidelines.

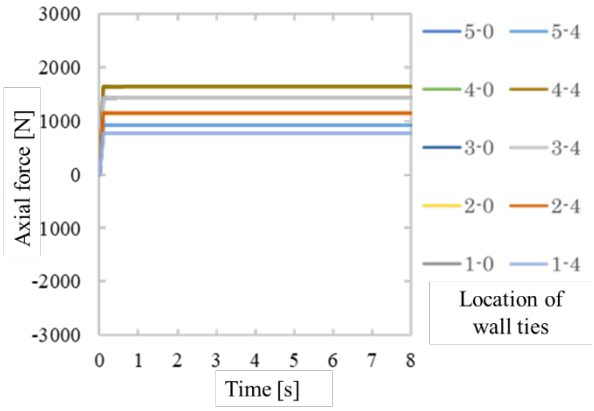

Figure 30. Axial forces acting on the wall ties under wind loads calculated based on the Safety Technical Guidelines.

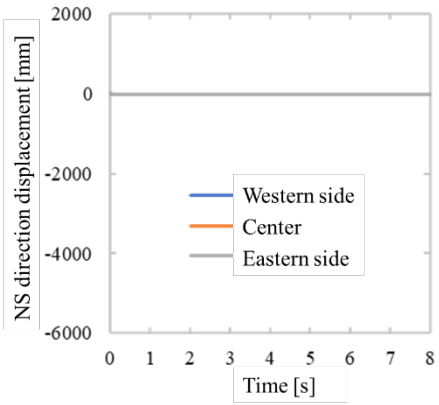

Figure 31. NS direction displacements at the top of the scaffolding under wind loads calculated based on the Safety Technical Guidelines.

1) The results of the fluid analysis showed that flow separation occurred from the upwind side of the scaffolding and expanded to the downwind side with time. The wind load acted in the direction of pulling the scaffolding off the building.

2) The structural analysis using the wind loads obtained from the fluid analysis indicated that the scaffolding collapsed because its wall ties were pulled out on the windward side. The axial forces on the wall ties attached to layers 1 to 3 were particularly large, suggesting the need to reinforce the middle and lower layers of the scaffolding, which are affected by the flow separation.

3) The wind loads calculated from the fluid analysis and Safety Technical Guidelines exhibited significant differences in trend. The wind loads calculated from the fluid analysis were complex owing to flow separation and instantaneous flow, while those calculated by the Safety Technical Guidelines were constant, as they do not take those factors into account.

As described above, the one-way fluid–structure coupled analysis revealed that even if the scaffolding is determined to be safe according to the Safety Technical Guidelines, the wind loads caused by the complex flow effects may lead to the collapse of the scaffolding. The anchors for the wall ties may need at least 160% reinforcement to overcome those effects, or the number of wall ties should be increased to at least 160% of the original number, to reinforce the middle and lower layers of the scaffoldings.

6. References

[1] Tokyo Shinbun, Toyoko Line trains resume operation after trackside scaffold collapses, affecting 170,000 passengers. March 3, 2021(in Japanese). https://www.tokyo-np.co.jp/article/89171.

[2] Laitinen H, Marjamäki M, Päivärinta K. The validity of the TR safety observation method on building construction. Accid Anal Prev. 1999; 31(5): 463–472. https://doi.org/10.1016/S0001-4575(98)00084-0.

[3] Whitaker SM, Graves RJ, James M, McCann P. Safety with access scaffolds: Development of a prototype decision aid based on accident analysis. J Safety Res. 2003; 34 (3): 249–261. https://doi.org/10.1016/S0022-4375(03)00025-2.

[4] Dogan E, Yurdusev MA, Yildizel SA, Calis G. Investigation of scaffolding accident in a construction site: A case study analysis. Eng Fail Anal. 2021; 120: 105108. https://doi.org/10.1016/j.engfailanal.2020.105108.

[5] Halperin KM, McCann M. An evaluation of scaffold safety at construction sites. J Safety Res. 2004; 35(2): 141–150. https://doi.org/10.1016/j.jsr.2003.11.004.

[6] Rubio-Romero JC, Rubio Gámez MC, Carrillo-Castrillo JA. Analysis of the safety conditions of scaffolding on construction sites. Saf Sci. 2013; 55: 160–164. https://doi.org/10.1016/j.ssci.2013.01.006.

[7] Weesner LB, Jones HL. Experimental and analytical capacity of frame scaffolding. Eng Struct. 2001; 23: 592–599. https://doi.org/10.1016/S0141-0296(00)00087-0.

[8] Takanashi S, Ohdo K, Takahashi H. Strength of scaffolding tie-bar anchors fixed to ALC panels. Occup Saf Health Res. 2009; 2(2): 85–90. https://doi.org/10.2486/josh.2.85.

[9] Wang C, Zhang H, Rasmussen KJR, Reynolds J, Yan S. System reliability-based limit state design of support scaffolding systems. Eng Struct. 2020; 226: 110677. https://doi.org/10.1016/j.engstruct.2020.110677.

[10] Lipecki T, Jamińska-Gadomska P, Błazik-Borowa E. Wind load on façade scaffolding without protective cover – Eurocode and in-situ measurement approaches. J Build Eng. 2021; 42: 102516. https://doi.org/10.1016/j.jobe.2021.102516.

[11] Peng JL. Structural modeling and design considerations for double-layer shoring systems. J Construct Eng Manage. 2004; 130(3): 368–377. https://doi.org/10.1061/(ASCE)0733-9364(2004)130:3(368).

[12] Yu W, Chung K. Prediction on load carrying capacities of multi-storey door-type modular steel scaffolds. Steel Compos Struct. 2004; 4(6): 471–487. https://doi.org/10.12989/scs.2004.4.6.471.

[13] Zhang H, Rasmussen KJR. System-based design for steel scaffold structures using advanced analysis. J Constr Steel Res. 2013; 89: 1–8. https://doi.org/10.1016/j.jcsr.2013.05.014.

[14] Peng JL, Ho CM, Chan SL, Chen WF. Stability study on structural systems assembled by system scaffolds. J Constr Steel Res. 2017; 137: 135–151. https://doi.org/10.1016/j.jcsr.2017.06.004.

[15] Błazik-Borowa E, Geryło R, Wielgos P. The probability of a scaffolding failure on a construction site. Eng Fail Anal. 2022; 131: 105864. https://doi.org/10.1016/j.engfailanal.2021.105864.

[16] Scaffolding and Construction Equipment Association of Japan. Revised Safety Technical Guidelines of Scaffoldings against Wind Loads, 2019.

[17] OpenFOAM. https://openfoam.org/.

[18] Isobe D. Progressive Collapse Analysis of Structures: Numerical Codes and Applications. Elsevier, eBook. 2017.

[19] Society of Open CAE. Numerical analysis of heat transfer and flow using OpenFOAM, 2nd Ed. 2021.

[20] Yakhot V, Orszag SA. Renormalization group analysis of turbulence. I. Basic theory. J Sci Comput. 1986; 1: 3–51. https://doi.org/10.1007/BF01061452.

[21] Matsuyama T, Ohashi M, Noda H, Nagai N, Watakabe M, Okabe M. CFD Analysis of Flowfield around a Cubic Model and Wind Pressure on the Walls. Summaries of technical papers of annual meeting. 2002, Architectural Institute of Japan. 157–158.

[22] Ministry of Health, Labour and Welfare, Japan. Occupational Safety and Health Regulations, Vol. 2, Chapter 10, Article 570, Steel pipe scaffolding.

[23] JISA8951. Steel pipe scaffolding, 2016.